



# Global Biogeochemical Cycles

## RESEARCH ARTICLE

10.1002/2013GB004683

### Key Points:

- Outgassing intensification linked to coastal topographic features
- Near-shore outgassing balanced by offshore absorption
- Carbon fluxes most sensitive to horizontal resolution for 35–40N

### Correspondence to:

J. Fiechter,  
fiechter@ucsc.edu

### Citation:

Fiechter, J., E. N. Curchitser, C. A. Edwards, F. Chai, N. L. Goebel, and F. P. Chavez (2014), Air-sea CO<sub>2</sub> fluxes in the California Current: Impacts of model resolution and coastal topography, *Global Biogeochem. Cycles*, 28, 371–385, doi:10.1002/2013GB004683.

Received 2 JUL 2013

Accepted 9 MAR 2014

Accepted article online 13 MAR 2014

Published online 4 APR 2014

## Air-sea CO<sub>2</sub> fluxes in the California Current: Impacts of model resolution and coastal topography

Jerome Fiechter<sup>1</sup>, Enrique N. Curchitser<sup>2</sup>, Christopher A. Edwards<sup>3</sup>, Fei Chai<sup>4</sup>, Nicole L. Goebel<sup>3</sup>, and Francisco P. Chavez<sup>5</sup>

<sup>1</sup>Institute of Marine Sciences, University of California, Santa Cruz, California, USA, <sup>2</sup>Institute of Marine and Coastal Sciences, State University of N. J. Rutgers, New Brunswick, New Jersey, USA, <sup>3</sup>Ocean Sciences Department, University of California, Santa Cruz, California, USA, <sup>4</sup>School of Marine Sciences, University of Maine, Orono, Maine, USA, <sup>5</sup>Monterey Bay Aquarium Research Institute, Moss Landing, California, USA

**Abstract** The present study uses a suite of coupled physical-biogeochemical model simulations at 1/3°, 1/10°, and 1/30° to assess the impact of horizontal resolution on air-sea CO<sub>2</sub> fluxes in the California Current System (CCS), a relevant issue for downscaling between coarser resolution global climate models and higher resolution regional models. The results demonstrate that horizontal resolution is important to reproduce the sharp transition between near-shore outgassing and offshore absorption, as well as to resolve regions of enhanced near-shore outgassing in the lee of capes. The width of the outgassing region is overestimated when horizontal resolution is not eddy resolving (i.e., 1/3°) but becomes more dependent on shelf topography for eddy-resolving simulations (i.e., 1/10° and 1/30°). Enhanced near-shore outgassing is associated with a local increase in wind-driven upwelling in the lee of capes (i.e., expansion fans), meaning that sufficient horizontal resolution is needed both in the ocean circulation model and in the wind field forcing the model. From a global carbon budget perspective, the model indicates that biological production generates sufficient absorption within a few hundred kilometers of the coast to offset near-shore outgassing, which is consistent with the notion that midlatitude eastern boundary current upwelling systems act both as a sink and source for atmospheric CO<sub>2</sub>. Based on the 1/30° solution, the CCS between 35 and 45 N and out to 600 km offshore is a net carbon sink of approximately 6 TgC yr<sup>-1</sup>, with the 1/10° solution underestimating this value by less than 10% and the 1/3° solution by a factor of 3.

## 1. Introduction

Accurate predictions of air-sea CO<sub>2</sub> fluxes along continental margins are critical to understand the role of the coastal ocean in regulating the Earth's global carbon budget. While recent studies point out the impact of coastal ocean physical and biogeochemical processes on the carbon cycle [e.g., Fennel *et al.*, 2008; Hofmann *et al.*, 2011], the generally accepted estimates of global oceanic uptake of anthropogenic CO<sub>2</sub> (approximately 2 PgC yr<sup>-1</sup>) [Sabine *et al.*, 2004; Mikaloff-Fletcher *et al.*, 2006] do not fully account for the contributions of continental margins. The need to properly resolve coastal ocean processes is further warranted by the fact that continental shelves can act either as a source or sink for atmospheric CO<sub>2</sub>. For example, existing annual air-sea CO<sub>2</sub> flux data suggest significant latitudinal variability in carbon exchange in the California Current System (CCS) off the west coast of North America, with net outgassing on the southern CCS shelf and net uptake on the northern CCS shelf [Cai *et al.*, 2006]. Recent estimates based on observed and simulated carbon exchange in the CCS indicate that the region acts as a weak sink from atmospheric CO<sub>2</sub>, but the exact magnitude is not clearly established with values ranging from approximately 1 ± 4 TgC yr<sup>-1</sup> [Turi *et al.*, 2013] to 14 TgC yr<sup>-1</sup> [Hales *et al.*, 2012].

As one of the four main eastern boundary current upwelling systems, the CCS experiences high rates of biological productivity, biogeochemical cycling, and air-sea CO<sub>2</sub> exchange [Chavez *et al.*, 2007; Pennington *et al.*, 2009]. Because nutrient-rich upwelled waters also contain elevated amounts of dissolved inorganic carbon (DIC), the CCS continental shelf can act both a source (via newly upwelled waters) and sink (via newly generated primary production) for atmospheric CO<sub>2</sub>. For example, in situ measurements off Oregon during May–August 2001 suggest that shelf waters were a net sink for CO<sub>2</sub> during the summer upwelling season, although intense outgassing was observed episodically over a narrow coastal band [Hales *et al.*, 2005].

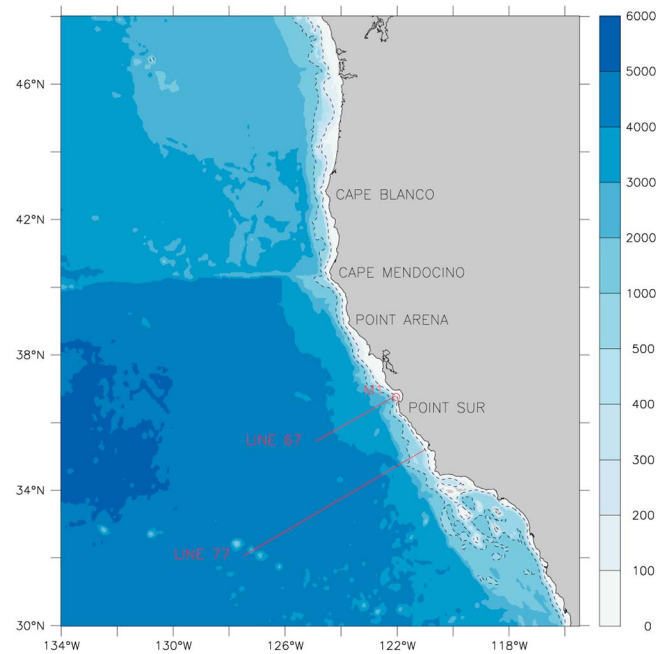


**Figure 1.** Model domain for the California Current Region with bottom topography (m). Dashed contours represent the model 200 and 1000 m isobaths. The locations of CALCOFI Line 77, MBARI Line 67, and MBARI M1 station are also indicated (red lines and circle).

Significant alongshelf  $p\text{CO}_2$  gradients were also observed in the same region during upwelling conditions, with the shelf region directly north (south) of Cape Blanco (near  $43^\circ\text{N}$ ) acting as a sink (source) of  $\text{CO}_2$  for the atmosphere [van Geen *et al.*, 2000].

The main objective of the present work is to use a suite of coupled physical-biogeochemical simulations to investigate the impact of horizontal model resolution on air-sea  $\text{CO}_2$  fluxes in the CCS. Understanding the accuracy with which coastal ocean processes need to be resolved to achieve robust predictions of carbon exchange is particularly relevant to upscaling/downscaling between global climate models and regional models. Because of the extreme narrowness of the continental shelf along the west coast of North America, a minimum horizontal resolution of 10 km is needed to resolve the dominant physical processes controlling upwelling dynamics

[Marchesiello *et al.*, 2003; Veneziani *et al.*, 2009], which poses a significant challenge for coarser resolution global climate models. Furthermore, the California Current transition zone [Kosro *et al.*, 1991], located between the coastal upwelling region and the core of the California Current 100 to 300 km offshore, is influenced by mesoscale eddy activity, which has been identified as a mechanism limiting primary production in eastern boundary current systems [Gruber *et al.*, 2011]. Accurately representing the impact of mesoscale features on the width of the coastal upwelling zone is therefore expected to produce more realistic estimates of air-sea  $\text{CO}_2$  fluxes and net carbon exchange in the CCS.

## 2. Coupled Physical-Biogeochemical Model

### 2.1. Regional Ocean Circulation Model

The ocean circulation model for the CCS is an implementation of the Regional Ocean Modeling System (ROMS) [Haidvogel *et al.*, 2008; Shchepetkin and McWilliams, 2005] and ranges geographically from  $30^\circ\text{N}$  to  $48^\circ\text{N}$  and  $116^\circ\text{W}$  to  $134^\circ\text{W}$  (Figure 1). To investigate the role of spatial resolution on simulated air-sea  $\text{CO}_2$  fluxes, three horizontal grid resolutions are considered:  $1/3^\circ$  (approximately 30 km),  $1/10^\circ$  (approximately 10 km), and  $1/30^\circ$  (approximately 3 km). The vertical resolution is set to 42 nonuniform terrain-following levels regardless of horizontal grid spacing. The three CCS ROMS models are forced on all open boundaries by monthly averaged fields from the Simple Ocean Data Assimilation reanalysis [Carton *et al.*, 2000] to guarantee realistic transport values and temperature and salinity profiles. Radiation conditions [Flather, 1976] and a sponge layer are used to reduce numerical instabilities near the open boundaries. Surface forcing for the three CCS ROMS models is derived from the Coupled Ocean-Atmosphere Mesoscale Prediction System (COAMPS) [Hodur *et al.*, 2002]. COAMPS provides a complete and consistent set of daily atmospheric variables (winds, air temperature, sea level pressure, specific humidity, precipitation, and short-wave and downwelling long-wave radiation) on multiple nested grids with horizontal resolution ranging from 3 to 27 km. The highest grid resolutions (3 to 9 km) encompass most of California and Oregon, which allow the representation of complex wind structures typical of the CCS coastal region [Doyle, 1997]. Momentum, heat, and freshwater fluxes are calculated internally in ROMS using the COAMPS fields and a bulk flux formulation [Liu *et al.*, 1979; Fairall *et al.*, 1996].

## 2.2. Biogeochemical Model

The biogeochemical model is based on the 11-component North Pacific Ecosystem Model for Understanding Regional Oceanography (NEMURO) model [Kishi *et al.*, 2007]. In its default configuration, NEMURO includes three limiting macronutrients (nitrate, ammonium, and silicic acid), two phytoplankton size-classes (nanophytoplankton and diatoms), three zooplankton size-classes (microzooplankton, mesozooplankton, and predatory zooplankton), and three detritus pools (dissolved and particulate organic nitrogen and particulate silica). NEMURO uses nitrogen as the common “currency”, and for diatoms, silicon is converted to nitrogen using a fixed Si:N ratio. To differentiate between more turbid shelf waters and clear oceanic offshore waters, the light attenuation coefficient in NEMURO is set to vary as a function of total water depth and decreases linearly from  $0.08 \text{ m}^{-1}$  inshore of the 200 m isobath to  $0.04 \text{ m}^{-1}$  offshore of the 2000 m isobath. This correction accounts for light attenuation contributions in coastal waters (e.g., sediments and particulate organic matter) other than phytoplankton self-shading, which is explicitly accounted for in NEMURO. The variable light attenuation coefficient (based on water type I and IA/B) [Jerlov, 1976] helps achieve more realistic chlorophyll concentrations on the shelf by not overestimating light levels in the water column, while concurrently retaining the presence of a deep chlorophyll maximum offshore.

For the purpose of this study, NEMURO has been augmented with a carbon submodel (NEMURO-Carbon, hereafter referred to as “NEMC”) based on the formulation and parameterization of Hauri *et al.* [2013] by adding three compartments: dissolved inorganic carbon (DIC), alkalinity, and calcium carbonate ( $\text{CaCO}_3$ ). The equilibrium partial pressure of  $\text{CO}_2$  ( $p\text{CO}_2$ ) in surface seawater is computed following the numerical methods developed by the Ocean Carbon-Cycle Model Intercomparison Project [Najjar and Orr, 1999]. Using a bulk formula approach, the  $\text{CO}_2$  flux across the air-sea interface is then given by the following:

$$F = k s \Delta p\text{CO}_2$$

where  $k$  is the gas transfer velocity,  $s$  is the solubility of  $\text{CO}_2$  in sea water, and  $\Delta p\text{CO}_2$  is the partial pressure difference across the air-sea interface (atmospheric  $p\text{CO}_2$  is kept constant at 370 ppmv) [Fennel *et al.*, 2008]. The gas transfer velocity depends on surface wind speed and the Schmidt number for dissolved  $\text{CO}_2$  [Wanninkhof, 1992], while the solubility of  $\text{CO}_2$  in sea water at the surface varies as function of temperature and salinity [Weiss, 1974].

The biogeochemical model is coupled to the ocean circulation model by solving a transport equation in ROMS for each NEMC component at every time step. A vertical sinking velocity of  $40 \text{ m d}^{-1}$  is also applied to the nitrogen, silica, and carbon detritus. The initial and boundary conditions for nitrate and silicic acid are based on monthly climatological values from the World Ocean Atlas 2001 [Conkright and Boyer, 2002]. The initial and boundary conditions for DIC and alkalinity are based on annual means from the Global Ocean Data Analysis Project [Key *et al.*, 2004]. For lack of better information, the initial and boundary conditions for the other biogeochemical tracers are set to a small value.

## 3. Results

The results presented in this section are based on integrations of the coupled ROMS-NEMC models for 1999–2005, and the three cases considered are hereafter referred to as NEMC3 ( $1/3^\circ$  grid), NEMC10 ( $1/10^\circ$  grid), and NEMC30 ( $1/30^\circ$  grid). A 7 year spin-up was performed on each grid by repeating the first year of the simulation (1999) until reaching a stable seasonal cycle to ensure that physical and biogeochemical fields are not affected by initial condition adjustments.

### 3.1. Model-Data Comparison

Since an extensive evaluation of the  $1/10^\circ$  ROMS solution for several key physical variables (i.e., sea surface height and temperature, eddy kinetic energy, temperature and salinity vertical structure) has already been presented elsewhere [Broquet *et al.*, 2009; Veneziani *et al.*, 2009], the model-data comparison focuses on biogeochemical fields (i.e., nutrients, chlorophyll,  $p\text{CO}_2$ , and air-sea  $\text{CO}_2$  fluxes) to illustrate the impact of horizontal grid resolution on regional and seasonal variability. Phytoplankton concentrations from NEMURO in nitrogen units are converted to chlorophyll using a constant C:N Redfield ratio of  $6.6 \text{ mol C mol N}^{-1}$  and a

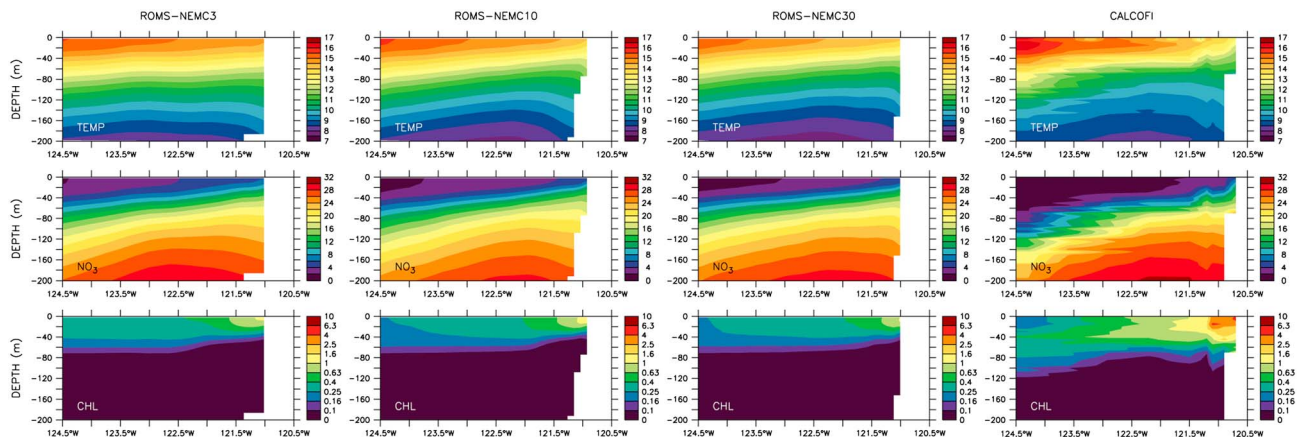


**Figure 2.** (top) Simulated and observed annual mean temperature ( $^{\circ}\text{C}$ ), (middle) nitrate concentrations ( $\text{mmol N m}^{-3}$ ), and (bottom) chlorophyll concentrations ( $\text{mg m}^{-3}$ ) along CALCOFI Line 77 (see Figure 1 for location). (from left to right) NEMC3, NEMC10, NEMC30, and observations.

variable phytoplankton Chl:C ratio based on an empirical relationship for phytoplankton under various temperature, light, and nutrient-limited growth conditions [Cloern *et al.*, 1995].

Vertical sections of annual mean temperature, nitrate, and chlorophyll concentrations along California Cooperative Oceanic Fisheries Investigations (CALCOFI) Line 77 (see Figure 1 for location) indicate that all three model solutions are in reasonable agreement with observed cross-shelf biophysical properties (Figure 2). For temperature and nitrate concentrations, simulated fields in the upper 200 m of the water column reproduce the magnitude and vertical structure (e.g., uplift of isotherms/isoclines near the coast) of their observed counterparts. For chlorophyll concentrations, simulated phytoplankton biomass is typically weaker and occurs at shallower depths than suggested by the observations. Lower biomass in the model solutions is partly explained by the fact that simulated chlorophyll concentrations represent an annual mean of monthly averaged values, while observed chlorophyll concentrations represent an annual mean of synoptic measurements. Magnitude discrepancies are also likely to occur when converting simulated phytoplankton concentrations to chlorophyll because of uncertainties in the Chl:C ratio.

Regional patterns and seasonal variability in simulated biogeochemical fields are evaluated more quantitatively by comparing the model solutions to remotely sensed observations from the Sea-viewing Wide Field-of-view Sensor (SeaWiFS) for chlorophyll, as well as in situ measurements from the Lamont-Doherty Earth Observatory (LDEO) global surface  $p\text{CO}_2$  database [Takahashi *et al.*, 2013] and Surface Ocean  $\text{CO}_2$  Atlas (SOCAT) [Bakker *et al.*, 2013]. To facilitate model-data comparison, the LDEO and SOCAT observations were first normalized to a common year (chosen to be 2002, the midpoint year in the simulations) using a mean  $p\text{CO}_2$  increase rate of  $1.5 \mu\text{atm yr}^{-1}$  [Takahashi *et al.*, 2006] and then mapped with equal weight to a common  $0.5^{\circ} \times 0.5^{\circ}$  grid using Gaussian interpolation. To maintain a uniform sample size regardless of model resolution, simulated fields are interpolated to the observation grid prior to computing the statistics needed to summarize model-data agreement on the shelf (i.e., 0–100 km offshore) and in the basin (i.e., 100–600 km offshore) via Taylor diagrams [Taylor, 2001].

For chlorophyll, all three model solutions reproduce observed regional patterns and seasonal variations across the CCS (Figure 3). The most noticeable difference is the wider cross-shelf extent over which elevated phytoplankton biomass occurs in response to seasonal coastal upwelling in NEMC3 compared to NEMC10 and NEMC30. Based on the Taylor diagrams, increasing horizontal resolution improves annual mean spatial pattern correlation but worsens bias. Furthermore, simulated chlorophyll concentrations underestimate observed spatial variability over the entire domain. Despite the model-data discrepancies, all three solutions exhibit relatively low root-mean-square differences, with values of  $0.92$  to  $0.97 \text{ mg m}^{-3}$  on the shelf and  $0.09$  to  $0.1 \text{ mg m}^{-3}$  offshore.

For  $p\text{CO}_2$ , simulated fields reasonably reproduce observed zonal and meridional seasonal variations across the CCS (Figure 4), but discrepancies associated with the wider coastal upwelling zone in NEMC3 are exacerbated, especially during winter months. As a result, annual mean  $p\text{CO}_2$  values on the shelf exhibit a

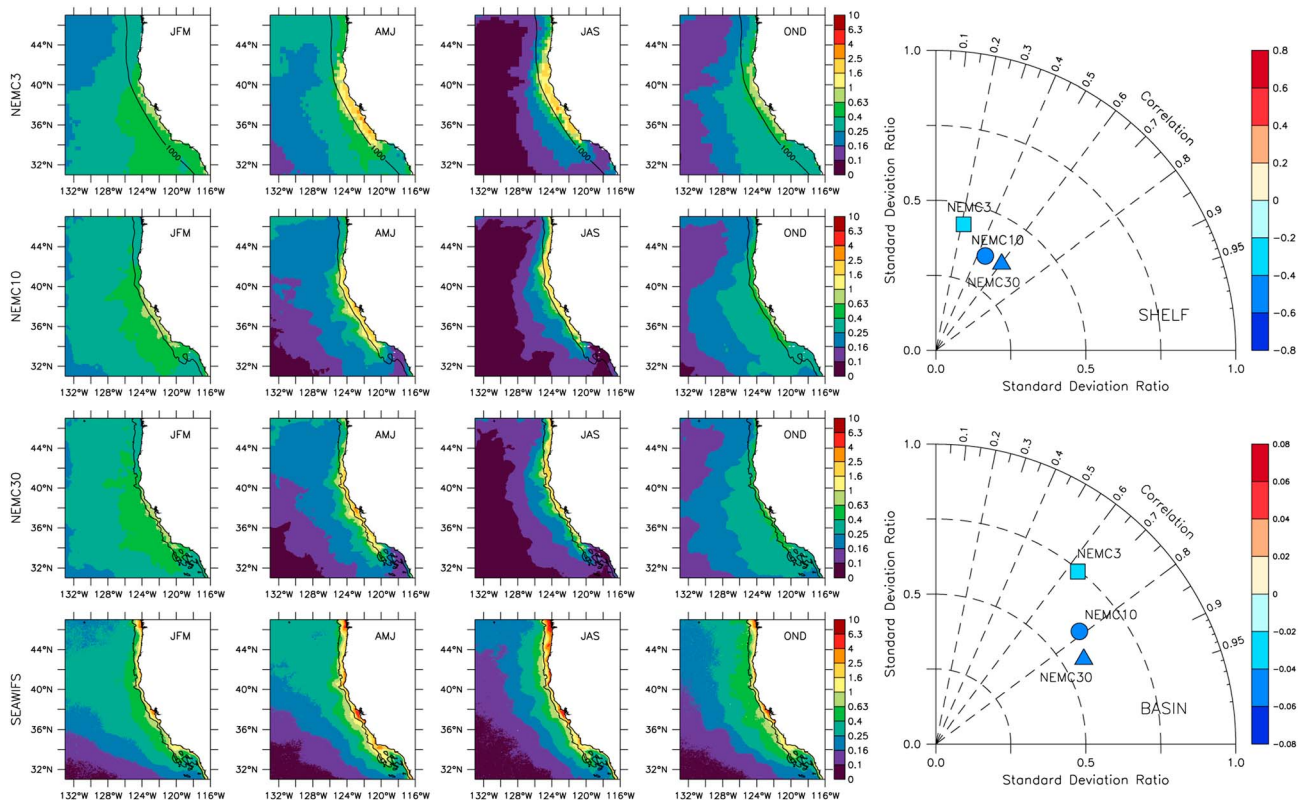


**Figure 3.** Simulated and observed seasonal mean climatological surface chlorophyll concentrations. (left column) Chlorophyll concentrations ( $\text{mg m}^{-3}$ ) for (from left to right) January–March (JFM), April–June (AMJ), July–September (JAS), and October–December (OND) based on (from top to bottom) NEMC3, NEMC10, NEMC30, and SeaWiFS; in all panels, the solid black line indicates the model 1000 m isobath. (right column) Taylor diagrams for (top) shelf (0–100 km offshore) and (bottom) basin (100–600 km offshore) chlorophyll concentrations from NEMC3 (squares), NEMC10 (triangles), and NEMC30 (circles); color scale represents bias in  $\text{mg m}^{-3}$ . In a Taylor diagram, radial distance represents the ratio of simulated to observed standard deviations and azimuthal angle represents model-data correlation. A perfect model solution would coincide with the (1, 1) location (i.e., standard deviation ratio and correlation equal to 1).

positive bias of 21 ppmv in NEMC3, compared to much lower biases of 2.8 ppmv for NEMC10 and 0.8 ppmv for NEMC30. While increasing horizontal resolution substantially improves model bias on the shelf, annual mean spatial pattern correlation remains largely unchanged for the three model solutions, with values of approximately 0.8. Similar conclusions hold for the offshore region, where increasing resolution reduces bias (7.5 ppmv for NEMC3 versus 1.9 ppmv for NEMC10 and  $-0.4$  ppmv for NEMC30) but does not significantly change correlation (approximately 0.5). Compared to observed values, simulated  $p\text{CO}_2$  values underestimate spatial variability on the shelf and overestimate it offshore. Despite all three model solutions having relatively similar root-mean-square differences with respect to the observations (37 to 41 ppmv on the shelf and 16 to 18 ppmv offshore), it is important to underscore the substantial bias reduction for NEMC10 and NEMC30 compared to NEMC3, as even relatively small  $p\text{CO}_2$  biases can reverse the sign of air-sea carbon exchange when differences relative to atmospheric conditions are considered.

While evaluating model solutions at the regional scale is a necessary step, most of the variability related to wind-driven coastal upwelling dynamics in the CCS occurs at smaller spatial and shorter temporal scales than domain-wide seasonal variations. To illustrate this point, simulated  $p\text{CO}_2$  values are compared to in situ measurements collected by the Monterey Bay Aquarium Research Institute (MBARI) [Pennington *et al.*, 2009] off central California (approximately  $36^\circ\text{N}$ ). At the M1 station (see Figure 1 for location), all three model solutions indicate strong synoptic (i.e., daily) variability, with ocean surface properties during peak upwelling season abruptly reaching values in excess of 200 ppmv above mean atmospheric conditions (Figure 5). Synoptic variability is typically higher for NEMC3 than for NEMC10 and NEMC30 and matches more closely that of the observations. In contrast, NEMC10 and NEMC30 provide better agreement with respect to interannual variability. For example, monthly mean observed  $\Delta p\text{CO}_2$  values were on average negative or near

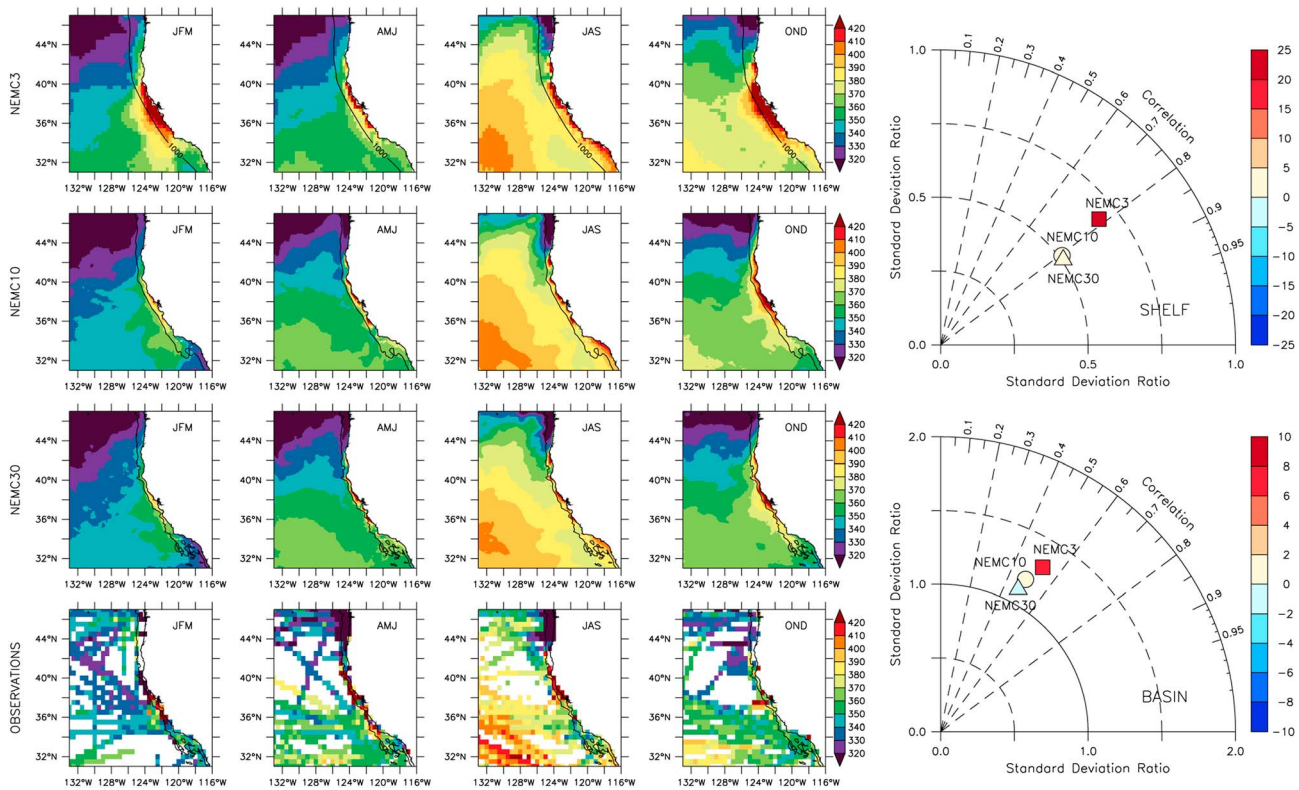


**Figure 4.** Simulated and observed seasonal mean climatological surface  $p\text{CO}_2$ . (left columns)  $p\text{CO}_2$  (ppmv) for (from left to right) January–March (JFM), April–June (AMJ), July–September (JAS), and October–December (OND) based on (from top to bottom) NEMC3, NEMC10, NEMC30, and LDEO/SOCAT; in all panels, the solid black line indicates the model 1000 m isobath. (right columns) Taylor diagrams for (top) shelf (0–100 km offshore) and (bottom) basin (100–600 km offshore)  $p\text{CO}_2$  from NEMC3 (squares), NEMC10 (triangles), and NEMC30 (circles); color scale represents bias in ppmv. For details on Taylor diagram construction, see Figure 3.

zero during 2000–2001 and more frequently positive during 2002–2004, a pattern generally reproduced by NEMC10 and NEMC30, but not by NEMC3. It should, however, be noted that observed  $\Delta p\text{CO}_2$  variability at M1 is modulated by local circulation patterns not adequately reproduced by the model solutions. In particular, the M1 station is located directly above Monterey Canyon, a submarine feature known to create significant upwelling variability, and too narrow for its impact to be captured in the simulations, even at 3 km horizontal resolution.

Although noticeable differences exist between  $\Delta p\text{CO}_2$  values at M1 from NEMC3, NEMC10, and NEMC30, the mean cross-shelf structure of air-sea  $\text{CO}_2$  exchange exhibits a much stronger dependence on horizontal model resolution (Figure 5, bottom). Compared to observed air-sea  $\text{CO}_2$  flux along Line 67 (see Figure 1 for location), the NEMC3 solution fails entirely to capture the transition point between shelf outgassing and offshore absorption, a direct consequence of the markedly wider upwelling zone at  $1/3^\circ$  resolution. The NEMC10 solution agrees more closely with observations in terms of flux magnitude, but it still overestimates the width of the outgassing region by 30–40 km. In comparison, the NEMC30 solution exhibits close agreement with the observed width and strength of the outgassing region. Model-data discrepancies inshore of 20 km are explained by the fact that Line 67 extends inside Monterey Bay, which biogeochemical properties are not accurately resolved by the model solutions.

### 3.2. Air-Sea $\text{CO}_2$ Flux Variability

Having established that the model solutions exhibit reasonable agreement with available observations, emphasis is placed on quantifying the impact of horizontal resolution on zonal and meridional air-sea  $\text{CO}_2$  flux variability and net carbon exchange in the CCS. Differences between the model solutions are first identified by considering annual mean  $\text{CO}_2$  fluxes, as well as the cross-shelf distance over which near-shore outgassing occurs (i.e., outgassing distance) and that over which outgassing is balanced by offshore

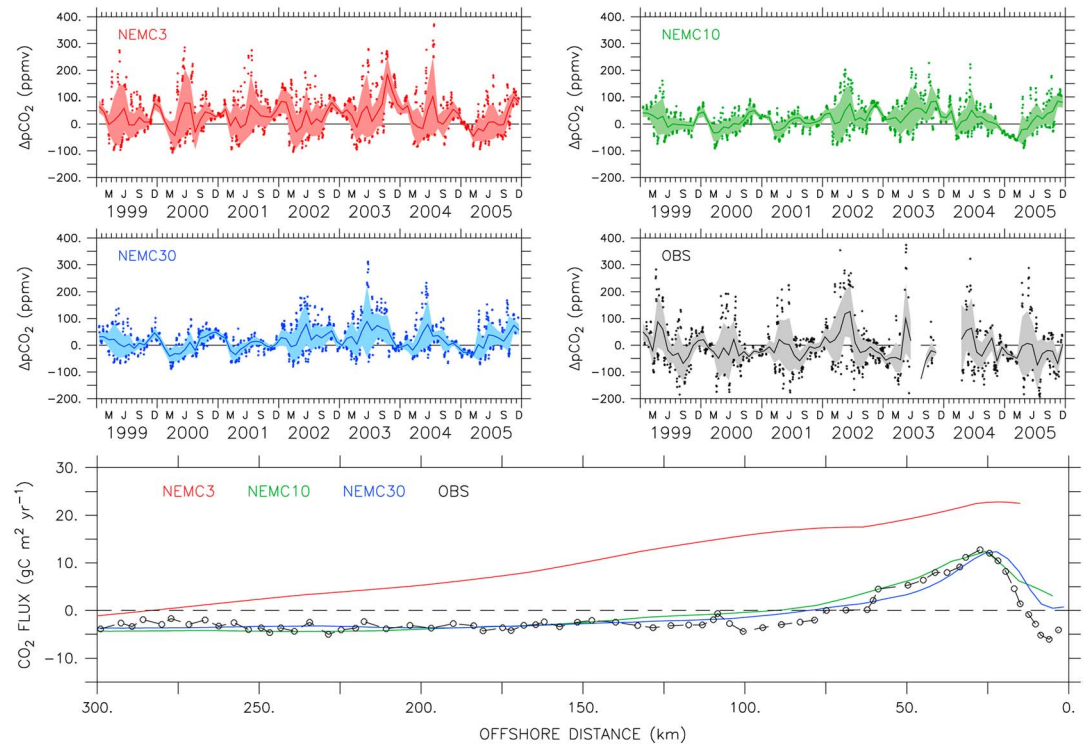


**Figure 5.** Simulated and observed  $\Delta p\text{CO}_2$  (ppmv) and air-sea  $\text{CO}_2$  fluxes ( $\text{gC m}^{-2} \text{yr}^{-1}$ ; positive is outgassing) at M1 station and along Line 67 (see Figure 1 for locations). (top and middle rows) Daily (symbols) and monthly (solid line)  $\Delta p\text{CO}_2$  from (top left) NEMC3, (top right) NEMC10, (middle left) NEMC30, and (middle right) observations; shaded area represents monthly  $\Delta p\text{CO}_2$  standard deviation; for figure clarity, only the daily values exceeding the monthly mean  $\pm$  one standard deviation are displayed. (bottom) The 1999–2005 mean  $\text{CO}_2$  flux along Line 67 from NEMC3 (red line), NEMC10 (green line), NEMC30 (blue line), and observations (black symbols).

absorption (i.e., equilibrium distance). As expected from the model-data comparison along MBARI Line 67, outgassing and equilibrium distances are much further offshore for NEMC3 than for NEMC10 and NEMC30, especially in the southern CCS (i.e., equatorward of  $40^\circ\text{N}$ ) (Figure 6). While the NEMC10 and NEMC30 solutions are qualitatively much closer, increasing horizontal resolution from  $1/10^\circ$  to  $1/30^\circ$  still has the nonnegligible effect of decreasing the average outgassing distance by approximately 22% (77 versus 94 km) and equilibrium distance by approximately 34% (331 versus 443 km) between  $35$  and  $40^\circ\text{N}$ . The impact of horizontal resolution is markedly less severe in the northern CCS (i.e.,  $40$ – $43^\circ\text{N}$ ), with a decrease in average

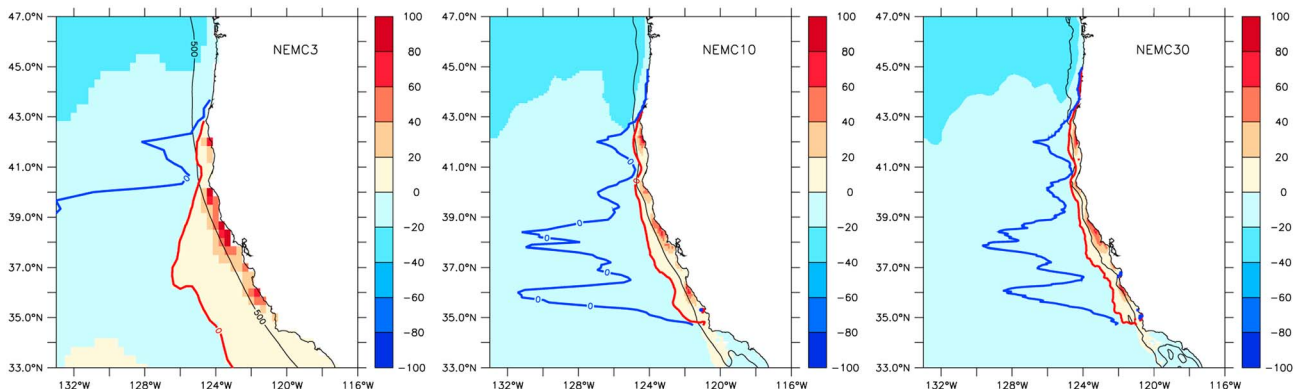


**Figure 6.** Annual mean air-sea  $\text{CO}_2$  fluxes ( $\text{gC m}^{-2} \text{yr}^{-1}$ ; positive is outgassing) from (left) NEMC3, (middle) NEMC10, and (right) NEMC30, with outgassing (red line) and equilibrium (blue line) distances indicated; the solid black line represents the model 500 m isobath.

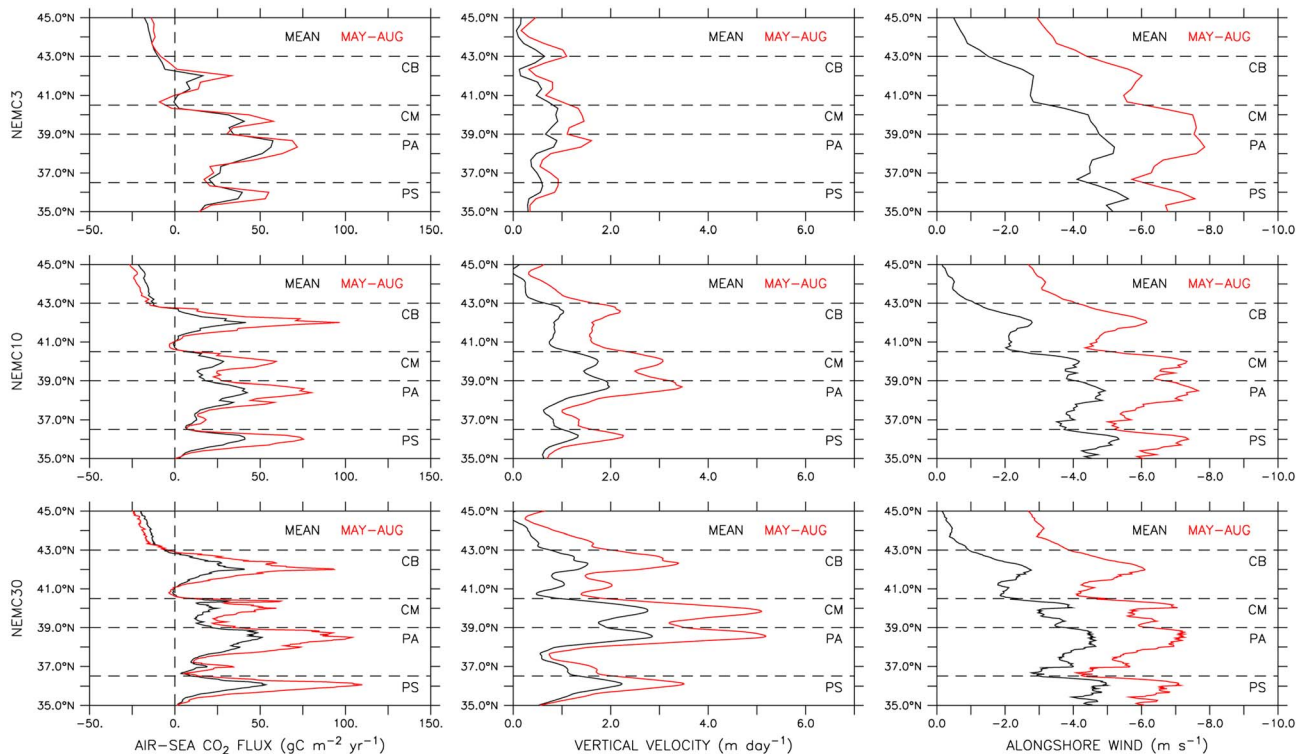


**Figure 7.** (left) Shelf-averaged annual (black lines) and May–August (red lines) mean climatological air-sea  $\text{CO}_2$  fluxes ( $\text{gC m}^{-2} \text{yr}^{-1}$ ; positive is outgassing), (middle) vertical velocity ( $\text{m d}^{-1}$ ) at 40 m depth, and (right) alongshore wind ( $\text{m s}^{-1}$ ; negative is equatorward) as a function of latitude from (top) NEMC3, (middle) NEMC10, and (lower) NEMC30; shelf is defined as inshore of the model 1000 m isobath. The horizontal dashed lines in each panel indicate the meridional locations of Cape Blanco (CB), Cape Mendocino (CM), Point Arena (PA) and Point Sur (PS).

outgassing distance by approximately 6% (31 versus 33 km) and equilibrium distance by approximately 8% (93 versus 100 km) between NEMC10 and NEMC30.

The NEMC10 and NEMC30 solutions also indicate that air-sea  $\text{CO}_2$  fluxes exhibit substantial meridional variability, as evidenced by the large latitudinal changes in equilibrium distances across the CCS. For example, the zonal distance over which carbon exchange equilibrates is on average 3 to 5 times further offshore at 36 and 38°N (400–500 km) than at 37 and 39°N (approximately 100 km). Since these differences are not directly related to similar changes in outgassing distances, meridional variability for the offshore equilibrium distance must be associated with variations in the magnitude of near-shore air-sea  $\text{CO}_2$  fluxes (i.e., for a given width of the outgassing region, larger equilibrium distances mean stronger near-shore outgassing). The occurrence of locally intensified upwelling centers on the shelf is also evidenced by regions of enhanced air-sea  $\text{CO}_2$  fluxes (i.e., annual means in the range of 60–100  $\text{gC m}^{-2} \text{yr}^{-1}$ ) near the latitudes at which equilibrium distance increases.

Meridional variability in upwelling intensity is further examined by considering zonally averaged carbon exchange on the shelf (i.e., inshore of the model 1000 m isobath) as a function of latitude. Simulated climatological (1999–2005) air-sea  $\text{CO}_2$  fluxes identify four subregions where enhanced near-shore outgassing occurs (Figure 7, left column). Outgassing intensification at these locations during peak upwelling season (i.e., May–August; based on peak upwelling-favorable, alongshore winds) is particularly marked in NEMC10 and NEMC30, with peak values reaching 50 to 100  $\text{gC m}^{-2} \text{yr}^{-1}$ . Furthermore, enhanced outgassing conditions coincide with the latitudes at which equilibrium distance increases (see Figure 6) and are located directly equatorward of four major topographic features of the west coast of North America, namely Point Sur (36.5°N), Point Arena (39°N), Cape Mendocino (40.5°N), and Cape Blanco (43°N) (see Figure 1 for locations). The results also indicate that intensified air-sea carbon exchange is highly localized geographically, as evidenced by the narrow latitudinal extent (i.e., 50–100 km) over which peak outgassing occurs (Figure 7, left

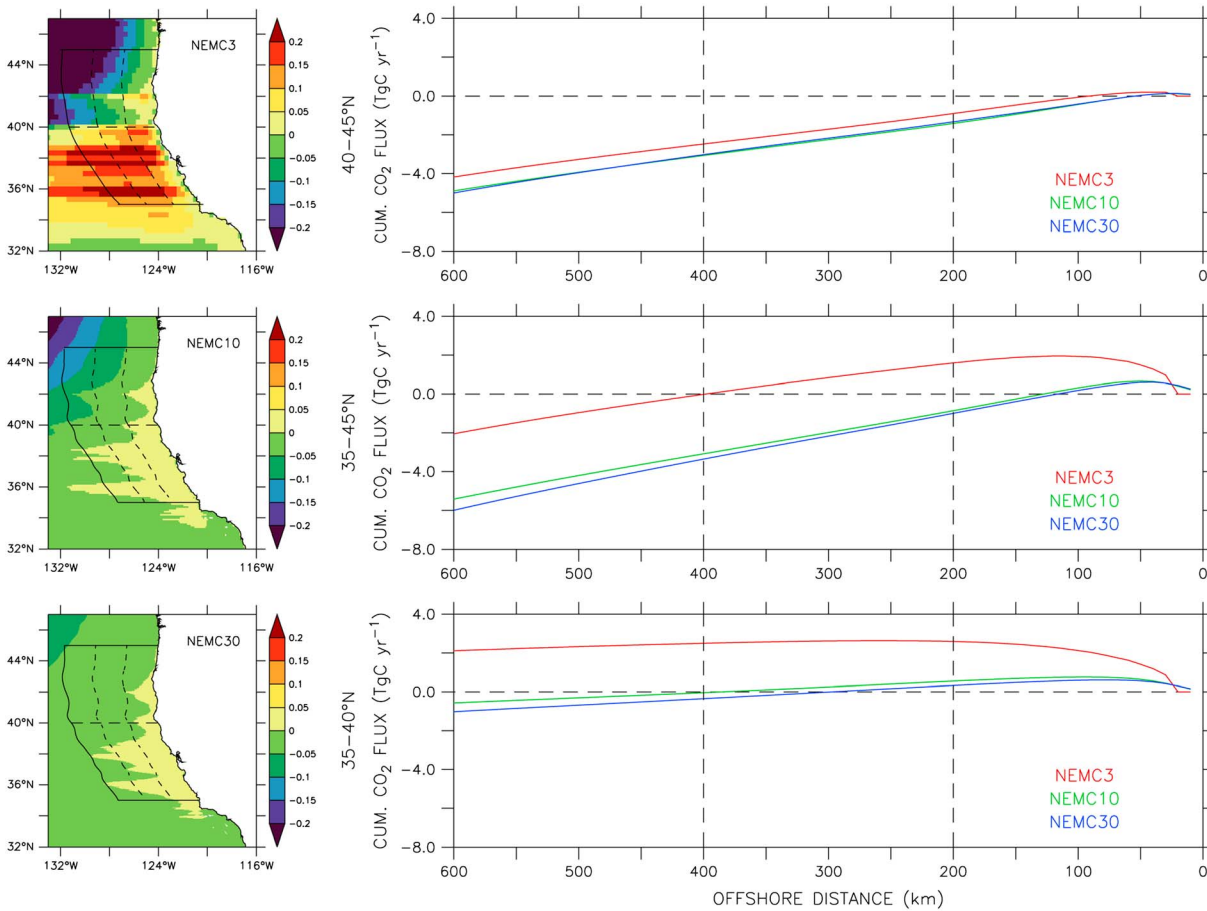


**Figure 8.** Zonally accumulated air-sea carbon fluxes ( $\text{TgC yr}^{-1}$ ; positive is outgassing) for the CCS from (top left) NEMC3, (middle left) NEMC10, and (bottom left) NEMC30; the solid black lines delimit the CCS region out to 600 km offshore; the dashed black lines delimit the southern and northern subregions and indicate offshore distances of 200 and 400 km for reference. (right) Zonally accumulated air-sea fluxes integrated meridionally over the (bottom) southern, (top) northern, and (middle) entire CCS from NEMC3 (red lines), NEMC10 (green lines), and NEMC30 (blue lines).

column). The locations at which air-sea  $\text{CO}_2$  fluxes are most intense coincide with regions of increased upwelling-favorable alongshore winds and near-shore vertical velocities (Figure 7, middle and right columns). The impact of horizontal model resolution on net carbon exchange is examined by zonally integrating air-sea  $\text{CO}_2$  fluxes out to 600 km offshore for three different regions: the southern ( $35\text{--}40^\circ\text{N}$ ), northern ( $40\text{--}45^\circ\text{N}$ ), and entire ( $35\text{--}45^\circ\text{N}$ ) CCS (Figure 8, left). The results indicate that sensitivity to horizontal resolution is highest in the southern CCS, which is consistent with earlier considerations based on outgassing and equilibrium distances. In fact, the NEMC3 solution yields an integrated carbon exchange of opposite sign (net outgassing) to those based on the NEMC10 and NEMC30 solutions (net absorption) (Figure 8, bottom right). Furthermore, increasing resolution from  $1/10^\circ$  to  $1/30^\circ$  essentially doubles absorption from about  $0.5 \text{ TgC yr}^{-1}$  for NEMC10 to  $1 \text{ TgC yr}^{-1}$  for NEMC30. In contrast, horizontal resolution plays a less important role in the northern CCS where NEMC10 and NEMC30 yield nearly identical contributions of approximately  $5 \text{ TgC yr}^{-1}$ , and NEMC3 underestimates that value by only 20% (Figure 8, top right). Because the southern CCS is close to neutral, air-sea carbon exchange for the entire CCS is primarily determined by the stronger absorption conditions occurring in the northern CCS (Figure 8, middle right). Based on the NEMC30 solution, the entire CCS ( $35\text{--}45^\circ\text{N}$ ) out to 600 km offshore is a net sink for atmospheric  $\text{CO}_2$  of approximately  $6 \text{ TgC yr}^{-1}$ , with roughly 80% of that value contributed by the northern CCS ( $40\text{--}45^\circ\text{N}$ ). While estimating the same budget from the  $1/10^\circ$  solution yields a difference of less than 10% compared to the  $1/30^\circ$  solution, calculating net air-sea carbon exchange using the  $1/3^\circ$  solution underestimates the overall sink contribution by a factor of 3.

#### 4. Discussion

The occurrence of enhanced near-shore outgassing directly equatorward of coastal topographic features in the simulations is consistent with existing observations in the southern and northern CCS. For example, in situ measurements off Oregon in August 1995 indicate that the shelf region directly south of Cape Blanco is a significant source of CO<sub>2</sub> for the atmosphere, with daily  $p\text{CO}_2$  values in the range of 500–700 ppmv [van Geen *et al.*, 2000]. Intense outgassing conditions ( $p\text{CO}_2 > 500$  ppmv) were also reported directly equatorward of Point Año Nuevo and Point Sur during a typical upwelling event near Monterey Bay, with particularly strong upwelling conditions during the 1999 La Niña period resulting in synoptic air-sea CO<sub>2</sub> fluxes of 100 to 500 gC m<sup>-2</sup> yr<sup>-1</sup> [Friederich *et al.*, 2002]. These values are generally comparable to simulated variability at MBARI M1 station (see Figure 5) which indicates daily  $p\text{CO}_2$  values above 550 ppmv and associated air-sea CO<sub>2</sub> fluxes in excess of 200 gC m<sup>-2</sup> yr<sup>-1</sup> during intense upwelling events. Because of the combined effects of increased wind speed (i.e., higher gas transfer velocity) and upwelling intensity (i.e., higher  $p\text{CO}_2$ ), the regions of enhanced outgassing identified in observed and simulated CO<sub>2</sub> fluxes may be particularly susceptible to potential changes in wind conditions in the CCS. In fact, a recent study on the impact of upwelling intensification on air-sea CO<sub>2</sub> fluxes in the CCS [Lachkar and Gruber, 2013] suggests that the meridional locations where outgassing is most increased under strengthening wind stress conditions are similar to those identified in the present study (i.e., directly equatorward of major coastal topographic features).

The importance of enhanced upwelling near coastal topographic features, and the constraint it imposes on model resolution to accurately reproduce physical and biogeochemical variability, is ubiquitous to eastern boundary current systems [e.g., Aristegui *et al.*, 2004; Renault *et al.*, 2012; van Geen *et al.*, 2000] and other regions of the world's ocean [e.g., Macdonald *et al.*, 2009]. The horizontal resolution requirements associated with capes also extend to a suitable representation of local wind patterns [e.g., Koračín *et al.*, 2004], as the spatial structure of near-shore winds has a profound impact on upwelling dynamics [Albert *et al.*, 2010; Capet *et al.*, 2004]. Recent studies also suggest that horizontal resolution is important offshore, where mesoscale eddy transport [Gruber *et al.*, 2011] and submesoscale filamentary features [Resplandy *et al.*, 2009] can substantially modulate air-sea carbon exchange. The following subsections discuss the main findings from the present study in terms of horizontal model resolution on the shelf and offshore, as well as its impact on estimating air-sea CO<sub>2</sub> fluxes in the CCS.

##### 4.1. Importance of Horizontal Model Resolution

With regard to horizontal resolution, the results identify two key processes: overall decrease in zonal outgassing distance with increasing resolution, and meridional variability of near-shore outgassing associated coastal topography. Consequently, it is worth isolating which specific processes are associated with these changes and how model resolution modulates them. For zonal outgassing distance, existing studies have identified offshore eddy kinetic energy (EKE) as a mechanism for reducing biological production and contracting the width of the CCS coastal upwelling zone [Gruber *et al.*, 2011]. However, an improved representation of bottom topography with increasing model resolution may also lead to more accurate upwelling intensity and water masses properties. Respective contributions can be separated by contrasting meridional variability for the following variables: outgassing distance, shelf break location (i.e., offshore distance of model 1000 m isobath), and EKE at 100 km offshore (Figure 9, top). The model solutions suggest that the decrease in outgassing distances between NEMC3 (not eddy resolving) and NEMC10 (eddy resolving) is primarily related to an increase in EKE offshore of the shelf break (Figure 9, bottom left), which is consistent with the upwelling zone contraction mechanism described by Gruber *et al.* [2011]. In contrast, outgassing distance differences between NEMC10 and NEMC30 coincide more closely with changes in shelf break location (i.e., a wider shelf leads to outgassing distances further offshore) (Figure 9, bottom right). This finding is generally consistent with the scaling argument for upwelling width presented by Estrade *et al.* [2008], whereby the width of the upwelling zone is inversely proportional to the slope of the continental shelf. Since shelf break location is defined here as the offshore distance of the model 1000 m isobath, it is also a direct measure of the continental shelf slope. As a result, a wider shelf at 1/10° horizontal resolution for a given latitude implies a weaker shelf slope, and therefore, a wider upwelling zone compared to the 1/30° solution.

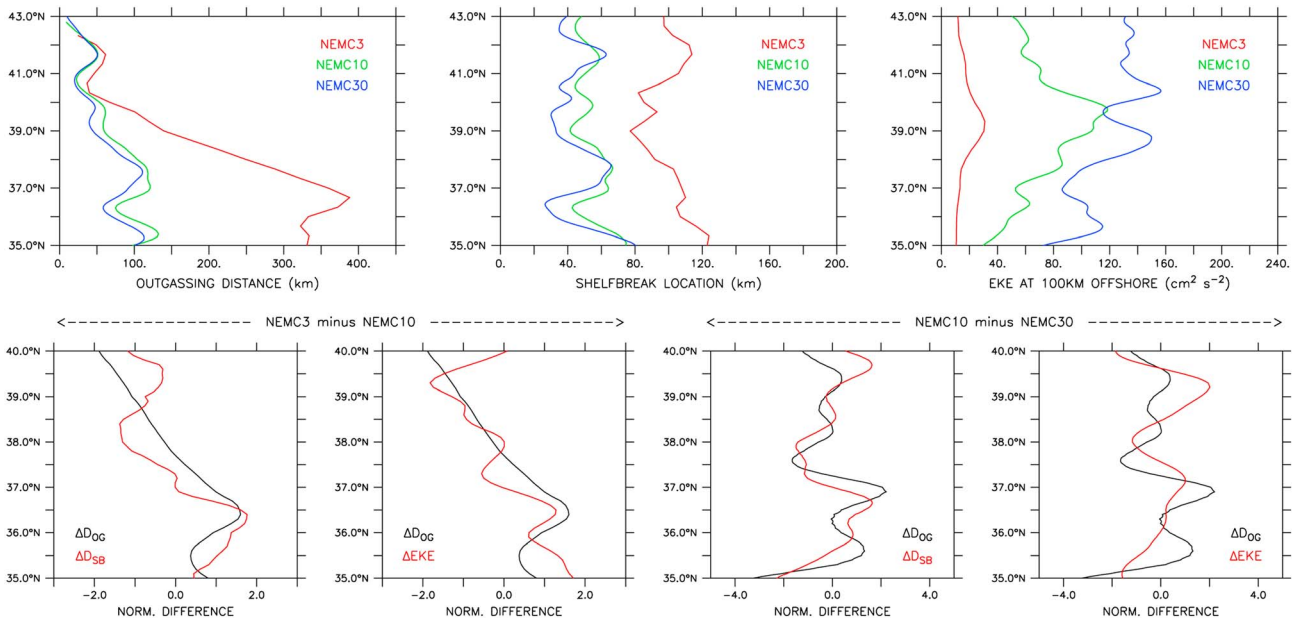


**Figure 9.** (top left) Outgassing distance ( $D_{OG}$ ), (top middle) shelf break location ( $D_{SB}$ ), and (top right) eddy kinetic energy at 100 km offshore (EKE) for NEMC3 (red), NEMC10 (green), and NEMC30 (blue); shelf break distance is defined as the offshore location of the model 1000 isobath. (bottom) Change in  $D_{OG}$  ( $\Delta D_{OG}$ ; black lines) versus changes in  $D_{SB}$  and EKE ( $\Delta D_{SB}$  and  $\Delta EKE$ ; red lines) (left) between NEMC3 and NEMC10 and (right) between NEMC10 and NEMC30; to facilitate comparison, differences are displayed as anomalies (meridional mean removed) normalized by their meridional standard deviation.

To further illustrate the mechanisms through which EKE and coastal upwelling width affect air-sea carbon exchange, mean cross-shore nutrient concentrations during the peak of the upwelling season (i.e., May–August) are contrasted along Line 67 near 37°N where differences in outgassing width between NEMC3, NEMC10, and NEMC30 are particularly marked (see Figure 9, top left). Comparing the NEMC3 and NEMC10 solutions indicates that differences in air-sea  $CO_2$  flux are highly correlated with differences in surface nitrate concentration (Figure 10, top left). Surface differences can in turn be related to differences in water column nitrate concentrations, with NEMC3 exhibiting higher values near the surface (upper 100 m) within approximately 250 km from the coast and lower values at depth (100–200 m) offshore (Figure 10, bottom left). This pattern

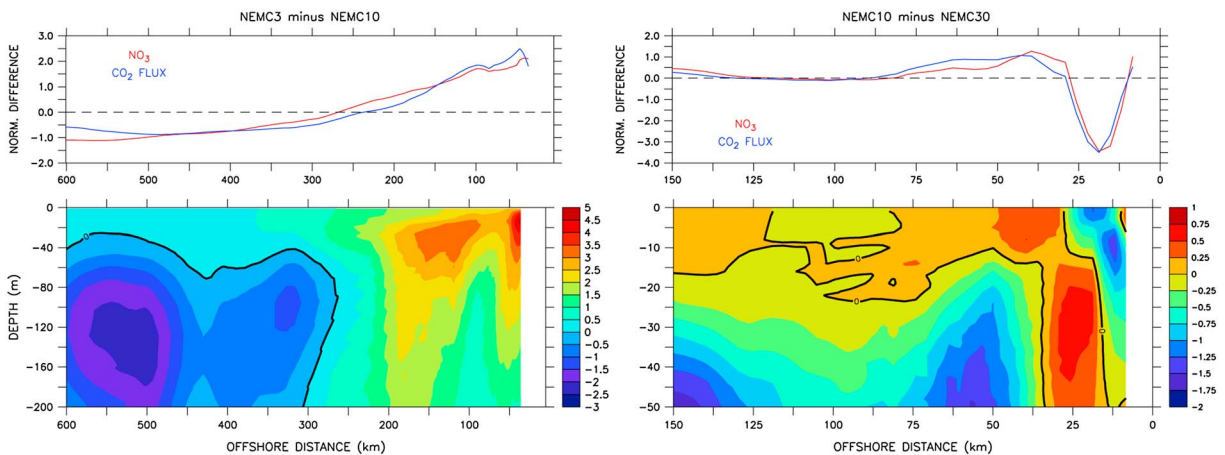


**Figure 10.** Air-sea  $CO_2$  flux and nitrate concentrations during May–August along Line 67 (see Figure 1 for location) expressed as differences (left) between NEMC3 and NEMC10 and (right) between NEMC10 and NEMC30. (top) Surface nitrate (blue) and  $CO_2$  flux (red) differences (with respect to cross-shore mean and normalized by cross-shore standard deviation). (bottom) Water column nitrate differences ( $mmol\ N\ m^{-3}$ ) with zero value indicated by black contour line. Note the different axis scales between Figures 10 (left) and 10 (right).

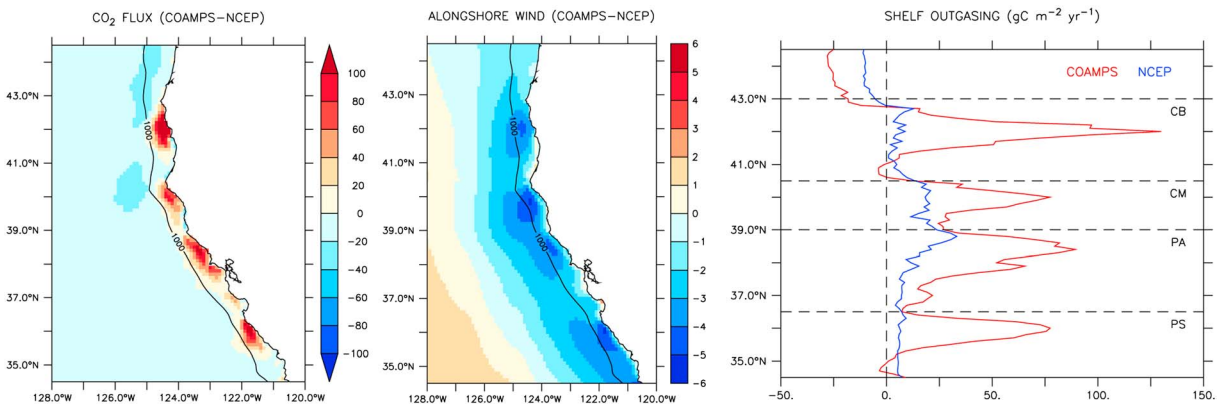


**Figure 11.** Impact of wind forcing resolution on air-sea  $\text{CO}_2$  flux ( $\text{gC m}^{-2} \text{yr}^{-1}$ ; positive is outgassing) for NEMC10. (left) COAMPS minus NCEP annual mean air-sea  $\text{CO}_2$  flux. (middle) COAMPS minus NCEP annual mean alongshore wind ( $\text{m s}^{-1}$ ; negative is equatorward). (right) Annual mean air-sea  $\text{CO}_2$  flux on the shelf (i.e., inshore of the model 1000 m isobath) for COAMPS (red) and NCEP (blue); the horizontal dashed lines indicate the meridional locations of Cape Blanco (CB), Cape Mendocino (CM), Point Arena (PA), and Point Sur (PS).

is consistent with that discussed by *Gruber et al.* [2011], whereby subduction by eddy transport offshore reduces nutrient concentrations in the coastal upwelling zone. Since DIC covaries with nutrients in upwelled waters, outgassing conditions in NEMC3 are thus more pronounced and extend further offshore than in NEMC10. Comparing the NEMC10 and NEMC30 solutions reveals a similar relationship between air-sea  $\text{CO}_2$  flux and surface nitrate concentrations, although differences occur primarily in the upwelling zone within approximately 80 km from the coast (Figure 10, top right). As evidenced by nitrate concentrations in the upper 50 m of the water column, NEMC30 exhibits a narrower, yet more intense, upwelling zone than NEMC10 (i.e., higher  $\text{NO}_3$  values within approximately 25 km from the coast and lower  $\text{NO}_3$  values between approximately 25 and 80 km) (Figure 10, bottom right). As a result, outgassing conditions in NEMC10 are weaker near the coast but extend further offshore compared to NEMC30. This pattern is consistent with the proposed upwelling width scaling of *Estrade et al.* [2008] and supports the assumption that a more detailed bottom topography at 3 km horizontal resolution (NEMC30) leads to a more accurate representation of coastal upwelling dynamics compared to 10 km horizontal resolution (NEMC10).

#### 4.2. Importance of Coastal Topographic Features

Regarding enhanced upwelling centers in the lee capes, one question is whether horizontal resolution is primarily needed in the wind field to account for expansion fans [e.g., *Koraćin et al.*, 2004], or if the magnitude of upwelling intensification is also dependent on horizontal resolution in the ocean circulation model. Given that the  $1/3^\circ$  grid poorly resolves coastal topography compared to the  $1/10^\circ$  and  $1/30^\circ$  grids, the fact that the NEMC3 solution broadly reproduces local outgassing intensification (see Figure 7, left column) suggests that atmospheric forcing is the dominant process. This hypothesis is further examined by forcing the  $1/10^\circ$  model with a coarse resolution wind product which does not resolve expansion fans in the lee of capes, such as the National Centers for Environmental Prediction/Department of Energy (NCEP-DOE) Reanalysis at  $1.9^\circ \times 1.9^\circ$  horizontal resolution [*Kanamitsu et al.*, 2002]. Although the NCEP-DOE Reanalysis has known shortcomings in upwelling regions [e.g., *Cambon et al.*, 2013], its intended use here is to illustrate the main differences between a low (NCEP) and high (COAMPS) resolution atmospheric product, as well as their impact on air-sea  $\text{CO}_2$  fluxes. Comparing air-sea  $\text{CO}_2$  fluxes and alongshore winds between the  $1/10^\circ$  COAMPS and NCEP solutions indicates that enhanced upwelling centers essentially vanish when the local impact of coastal topography on the wind field is not resolved (Figure 11), which suggests that the impact of horizontal resolution is primarily via atmospheric forcing (assuming that the ocean circulation model has sufficient resolution to produce correct upwelling dynamics).

The outgassing intensification occurring in the lee of capes is further reinforced by the fact that primary production associated with these upwelling centers is displaced equatorward under the effect of strong alongshore currents of approximately  $0.1 \text{ m s}^{-1}$  (Figure 12). Based on the NEMC10 solution, temperature, and  $p\text{CO}_2$  anomalies on the shelf (i.e., inshore of the model 1000 m isobath) during peak upwelling season

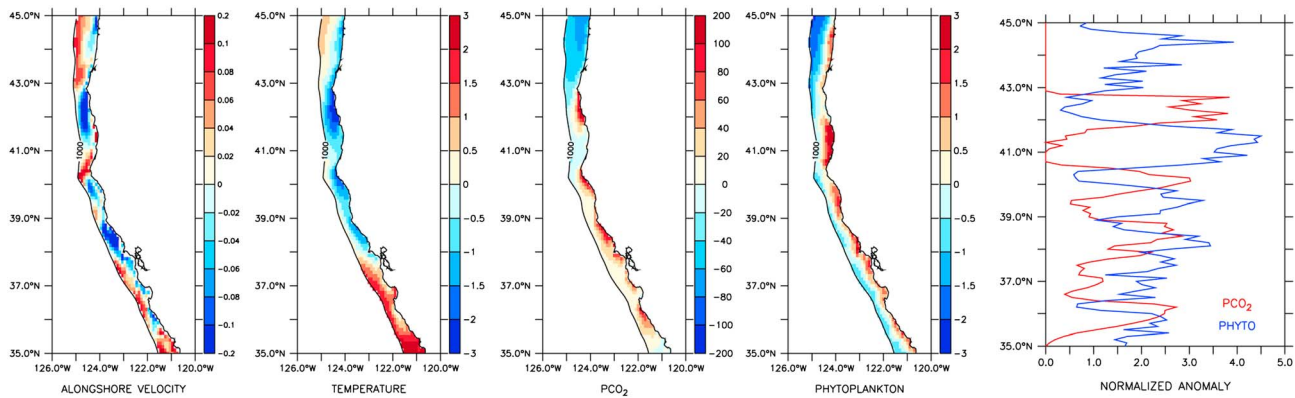


**Figure 12.** Shelf anomalies for surface (from left-to-right) alongshore velocity ( $\text{m s}^{-1}$ ; negative is equatorward), temperature ( $^{\circ}\text{C}$ ),  $p\text{CO}_2$  (ppmv), and phytoplankton concentration ( $\text{mmol N m}^{-3}$ ) from NEMC10 during May–August. (far right) Shelf-averaged positive  $p\text{CO}_2$  (red) and phytoplankton concentration (blue) anomalies (normalized by meridional standard deviation).

(i.e., May–August) are mainly collocated, which indicates that outgassing happens in the direct vicinity of the enhanced upwelling centers in the lee of capes. In contrast, the regions of elevated primary production associated with these upwelling centers occur approximately 100 km equatorward of the capes (Figure 12, far right), as nutrients are being advected alongshore at rates faster than the biological response (i.e., phytoplankton growth rates). This finding is consistent with previous modeling results from the CCS and Canary Current System [Lachkar and Gruber, 2011] and from the East Australian Current region [Macdonald *et al.*, 2009] indicating that near-shore residence time is an important factor controlling the compensation of elevated DIC concentrations in upwelled waters by primary production.

### 4.3. Regional Carbon Budget Estimates

Despite simplifications to the full array of processes impacting the carbon cycle on continental shelves, model-data comparisons against available biogeochemical observations indicate that the simulations reproduce the expected spatial and temporal patterns characterizing carbon exchange in the CCS at both regional/seasonal and local/synoptic scales. In terms of regionally integrated carbon exchange, the results are also in line with prior estimates for the CCS. While the net sink of  $6 \text{ TgC yr}^{-1}$  derived from NEMC30 for  $35\text{--}45^{\circ}\text{N}$  out to 600 km offshore is lower than the  $14 \text{ TgC yr}^{-1}$  sink calculated by Hales *et al.* [2012] for 1997–2005 from in situ  $p\text{CO}_2$  measurements within 370 km of the coastline, the difference may be partly attributed to the fact that the region considered by Hales *et al.* encompasses  $45\text{--}50^{\circ}\text{N}$ , which acts as a substantial sink of atmospheric  $\text{CO}_2$  throughout most of the year in their results. In contrast, a net sink of  $6 \text{ TgC yr}^{-1}$  is higher than the near-neutral conditions (net sink of  $0.9 \text{ TgC yr}^{-1}$ ) reported by Turi *et al.* [2013] based on numerical simulations, although their domain includes a larger portion of offshore oligotrophic waters where carbon is on average released to the atmosphere. The model solutions also differ in the magnitude of near-shore outgassing over the entire CCS, with the present study suggesting zero net exchange at approximately 100 km offshore whereas Turi *et al.* [2013] calculated a net integrated source of  $1.6 \text{ TgC yr}^{-1}$  over the same cross-shelf distance. This discrepancy may in part result from using climatological winds [Turi *et al.*, 2013] versus daily synoptic winds (this study) to force the coupled model.

While other processes, such as denitrification (which would increase seawater  $p\text{CO}_2$  and alkalinity) [Fennel *et al.*, 2008] and DIC/alkalinity seasonal variations at the open boundaries [Turi *et al.*, 2013], will presumably affect the magnitude of net carbon exchange estimates, the overall impact of horizontal resolution on air-sea  $\text{CO}_2$  fluxes identified in the simulations should not change significantly. These effects may also be secondary to those associated with changes in biogeochemical model parameterization (e.g., carbon cycling in upper ocean) and wind forcing, although more work is needed to identify their relative contributions. It should be noted that the present study focuses on the region between  $35^{\circ}\text{N}$  and  $45^{\circ}\text{N}$ , as the numerical solutions are expected to degrade near the model open boundaries at  $30^{\circ}\text{N}$  and  $48^{\circ}\text{N}$ . Furthermore, since the Columbia River outflow is not accounted for in the model, simulated physical and biological fields on the shelf north of  $45^{\circ}\text{N}$  may not reproduce observed variability when freshwater effects are important. Finally, it is left to future

work to determine if the  $1/30^\circ$  solution represents a converged estimate for carbon exchange in the CCS, as well as to explore the dependence of simulated air-sea  $\text{CO}_2$  fluxes on biological model parameterization (e.g., phytoplankton growth rates and particulate carbon sinking rates).

## 5. Conclusion

Results from a suite of coupled physical-biogeochemical simulations provide new insight on the impact of horizontal resolution on air-sea  $\text{CO}_2$  fluxes in the CCS. Differences between model solutions at  $1/3^\circ$ ,  $1/10^\circ$ , and  $1/30^\circ$  indicate that horizontal resolution is important for the following two reasons: (1) to reproduce the sharp transition between carbon outgassing on the shelf and absorption offshore and (2) to resolve regions of enhanced near-shore outgassing equatorward of capes. In terms of cross-shelf variability, the width of the outgassing region is largely overestimated when horizontal resolution is not eddy resolving (i.e.,  $1/3^\circ$ ). At eddy-resolving resolutions (i.e.,  $1/10^\circ$  and  $1/30^\circ$ ), the width of the outgassing region is more closely related to the accuracy with which the width of the continental shelf is represented. With regard to meridional variability, horizontal resolution is primarily needed to resolve wind-driven upwelling dynamics associated with wind expansion fans in the lee of capes, which points to the fact that horizontal resolution is not only important in the ocean circulation model but in the atmospheric wind field forcing the model. However, the results also indicate that simulated air-sea  $\text{CO}_2$  fluxes are markedly more sensitive to horizontal resolution in the southern CCS ( $35\text{--}40^\circ\text{N}$ ) than in the northern CCS ( $40\text{--}45^\circ\text{N}$ ). Based on the  $1/30^\circ$  solution, the sink nature of the CCS (approximately  $6 \text{ TgC yr}^{-1}$ ) is primarily determined by net absorption conditions in the northern CCS (approximately  $5 \text{ TgC yr}^{-1}$ ), as integrated carbon exchange in the southern CCS (approximately  $1 \text{ TgC yr}^{-1}$ ) is essentially neutral. Estimating the net carbon budget for the entire CCS from the  $1/10^\circ$  solution yields a difference of less than 10% compared to the  $1/30^\circ$  solution, while using the  $1/3^\circ$  solution underestimates the overall contribution by a factor of 3. Finally, the substantial amount of meridional variability present in near-shore  $\text{CO}_2$  fluxes cautions against using point measurements to quantify net carbon exchange in the CCS or other eastern boundary current upwelling regions.

## Acknowledgments

This research was primarily supported by a grant from the National Science Foundation Physical Oceanography Program (OCE-0961491). Any opinions, findings, and conclusions or recommendations expressed here are those of the authors and do not necessarily reflect the views of the National Science Foundation. Partial funding for this work was also provided by the NOAA-NMFS California Current Integrated Ecosystem Assessment program. SeaWiFS chlorophyll data are courtesy of the NOAA CoastWatch Program, NASA's Goddard Space Flight Center, and GeoEye. The CALCOFI Program is acknowledged for making available temperature, nutrient, and chlorophyll data along Line 77. NCEP\_Reanalysis 2 data were provided by the NOAA/OAR/ESRL PSD, Boulder, Colorado, USA. This research used ShaRCS, UC Shared Research Computing Services Cluster, which is technically supported by multiple UC IT divisions and managed by the University of California, Office of the President. The authors also thank Nicolas Gruber and one anonymous reviewer for their insightful and constructive comments. The model output used for this study can be obtained by contacting the lead author directly.

## References

- Albert, A., V. Echevin, M. Lévy, and O. Aumont (2010), Impact of nearshore wind stress curl on coastal circulation and primary productivity in the Peru upwelling system. *J. Geophys. Res.*, *115*, C12033, doi:10.1029/2010JC006569.
- Aristegui, J., E. D. Barton, P. Tett, M. F. Montero, M. García-Muñoz, G. Basterretxea, A. S. Cussatlegras, A. Ojeda, and D. de Armas (2004), Variability in plankton community structure, metabolism, and vertical carbon fluxes along an upwelling filament (Cape Juby, NW Africa). *Prog. Oceanogr.*, *62*, 95–113.
- Bakker, D. C. E., et al. (2013), An update to the surface ocean  $\text{CO}_2$  atlas (SOCAT version 2). *Earth Syst. Sci. Data Discuss.*, *6*, 465–512, doi:10.5194/esddd-6-465-2013.
- Broquet, G., C. A. Edwards, A. M. Moore, B. S. Powell, M. Veneziana, and J. D. Doyle (2009), Application of 4D-variational data assimilation to the California Current System. *Dyn. Atmos. Oceans*, *48*, 69–92, doi:10.1016/j.dynatmoce.2009.03.001.
- Cai, W.-J., Dai, M., and Wang, Y. (2006), Air-sea exchange of carbon dioxide in ocean margins: A province-based synthesis. *Geophys. Res. Lett.*, *33*, L12603, doi:10.1029/2006GL026219.
- Cambon, G., K. Goubanova, P. Marchesiello, B. Dewitte, S. Illig, and V. Echevin (2013), Assessing the impact of downscaled winds on a regional ocean model simulation of the Humboldt system. *Ocean Model.*, *65*, 11–24, doi:10.1016/j.ocemod.2013.01.007.
- Capet, X., P. Marchesiello, and J. McWilliams (2004), Upwelling response to coastal wind profiles. *Geophys. Res. Lett.*, *31*, L13309, doi:10.1029/2004GL020303.
- Carton, J. A., G. Chepurin, and X. Cao (2000), A Simple Ocean Data Assimilation analysis of the global upper ocean 1950–1995. Part 2: Results. *J. Phys. Oceanogr.*, *30*, 311–326.
- Chavez, F. P., T. Takahashi, W.-J. Cai, G. Friederich, B. Hales, R. Wanninkhof, and R. A. Feely (2007), Coastal oceans, in *The First State of the Carbon Cycle Report (SOCCR): The North American Carbon Budget and Implications for the Global Carbon Cycle. A Report by the U.S. Climate Change Science Program and the Subcommittee on Global Change Research*, edited by A. W. King et al., pp. 157–166, National Oceanic and Atmospheric Administration, Natl. Clim. Data Cent., Asheville, N. C.
- Cloern, J. E., C. Grenz, and L. Videgar-Lucas (1995), An empirical model of the phytoplankton chlorophyll: Carbon ratio – the conversion factor between productivity and growth rate. *Limnol. Oceanogr.*, *40*(7), 1313–1321.
- Conkright, M. E., and T. P. Boyer (2002), *World Ocean Atlas 2001: Objective Analyses, Data Statistics, and Figures*, pp. 17, CD-ROM documentation, Natl. Oceanogr. Data Cent., Silver Spring, Md.
- Doyle, J. D. (1997), The influence of mesoscale orography on a coastal jet and rainband. *Mon. Weather Rev.*, *125*, 1465–1488.
- Estrade, P., P. Marchesiello, A. C. De Verdière, and C. Roy (2008), Cross-shelf structure of coastal upwelling: A two-dimensional extension of Ekman's theory and a mechanism for inner shelf upwelling shut down. *J. Mar. Res.*, *66*(5), 589–616, doi:10.1357/002224008787536790.
- Fairall, C. W., E. F. Bradley, D. P. Rogers, J. B. Edson, and G. S. Young (1996), Bulk parameterization of air-sea fluxes for tropical ocean-global atmosphere Coupled-Ocean Atmosphere Response Experiment. *J. Geophys. Res.*, *101*, 3747–3764.
- Fennel, K., J. Wilkin, M. Previdi, and R. Najjar (2008), Denitrification effects on air-sea  $\text{CO}_2$  flux in the coastal ocean: Simulations for the northwest North Atlantic. *Geophys. Res. Lett.*, *35*, L24608, doi:10.1029/2008GL036147.
- Flather, R. A. (1976), A tidal model of the north-west European continental shelf. *Mem. Soc. R. Sci. Liege*, *6*(10), 141–164.

- Friederich, G. E., P. M. Walz, M. G. Burczynski, and F. P. Chavez (2002), Inorganic carbon in the central California upwelling system during the 1997–1999 El Niño-La Niña event, *Prog. Oceanogr.*, *54*, 185–203.
- Gruber, N., Z. Lachkar, H. Frenzel, P. Marchesiello, M. Münnich, J. C. McWilliams, T. Nagai, and G.-K. Plattner (2011), Eddy-induced reduction of biological production in eastern boundary upwelling systems, *Nat. Geosci.*, *4*, doi:10.1038/ngeo1273.
- Haidvogel, D. B., et al. (2008), Ocean forecasting in terrain-following coordinates: Formulation and skill assessment of the Regional Ocean Modeling System, *J. Comput. Phys.*, *227*, 3595–3624, doi:10.1016/j.jcp.2007.06.016.
- Hales, B., T. Takahashi, and L. Bandstra (2005), Atmospheric CO<sub>2</sub> uptake by a coastal upwelling system. *Global Biogeochem. Cycles*, *19*, GB1009, doi:10.1029/2004GB002295.
- Hales, B., P. G. Strutton, M. Saraceno, R. Letelier, T. Takahashi, R. Feely, C. Sabine, and F. Chavez (2012), Satellite-based prediction of pCO<sub>2</sub> in coastal waters of the eastern North Pacific, *Prog. Oceanogr.*, *103*, 1–15, doi:10.1016/j.pocean.2012.03.001.
- Hauri, C., N. Gruber, M. Vogt, S. C. Doney, R. A. Feely, Z. Lachkar, A. Leinweber, A. M. P. McDonnell, M. Münnich, and G.-K. Plattner (2013), Spatiotemporal variability and long-term trends of ocean acidification in the California Current System, *Biogeosciences*, *10*, 193–216, doi:10.5194/bg-10-193-2013.
- Hodur, R. M., J. Pullen, J. Cummings, X. Hong, J. D. Doyle, P. Martin, and M. A. Rennick (2002), The coupled ocean/atmosphere mesoscale prediction system (COAMPS), *Oceanography*, *15*, 88–98.
- Hofmann, E. E., et al. (2011), Modeling the dynamics of continental shelf carbon, *Annu. Rev. Mar. Sci.*, *3*, 93–122, doi:10.1146/annurev-marine-120709-142740.
- Jerlov, N. G. (1976), *Marine Optics*, pp. 230, Elsevier, Amsterdam, Netherlands.
- Kanamitsu, M., W. Ebisuzaki, J. Woollen, S.-K. Yang, J. J. Hnilo, M. Fiorino, and G. L. Potter (2002), NCEP-DEO AMIP-II Reanalysis (R-2), *Bull. Am. Meteorol. Soc.*, *83*, 1631–1643.
- Key, R. M., A. Kozyr, C. L. Sabine, K. Lee, R. Wanninkhof, J. L. Bullister, R. A. Feely, F. J. Millero, C. Mordy, and T.-H. Peng (2004), A global ocean carbon climatology: Results from Global Data Analysis Project (GLODAP). *Global Biogeochem. Cycles*, *18*, GB4031, doi:10.1029/2004GB002247.
- Kishi, M. J., et al. (2007), NEMURO – A lower trophic level model for the North Pacific marine ecosystem, *Ecol. Modell.*, *202*, 12–25, doi:10.1016/j.ecolmodel.2006.08.021.
- Koračin, D., C. E. Dorman, and E. P. Dever (2004), Coastal perturbations of marine-layer winds, wind stress, and wind stress curl along California and Baja California in June 1999, *J. Phys. Oceanogr.*, *34*, 1152–1173.
- Kosro, P. M., et al. (1991), The structure of the transition zone between coastal waters and the open ocean off northern California, winter and spring 1987, *J. Geophys. Res.*, *96*, 14,707–14,730.
- Lachkar, Z., and N. Gruber (2011), What controls biological production in coastal upwelling systems? Insights from a comparative modeling study, *Biogeosciences*, *8*, 2961–2976, doi:10.5194/bg-8-2961-2011.
- Lachkar, Z., and N. Gruber (2013), Response of biological production and air-sea CO<sub>2</sub> fluxes to upwelling intensification in the California and Canary Current Systems, *J. Mar. Syst.*, *109–110*, 149–160, doi:10.1016/j.marsys.2012.04.003.
- Liu, W. T., K. B. Katsaros, and J. A. Businger (1979), Bulk parameterization of the air-sea exchange of heat and water vapor including the molecular constraints at the interface, *J. Atmos. Sci.*, *36*, 1722–1735.
- Macdonald, H. S., M. E. Baird, and J. H. Middleton (2009), Effect of wind on continental shelf carbon fluxes off southeast Australia: A numerical model. *J. Geophys. Res.*, *114*, C05016, doi:10.1029/2008JC004946.
- Marchesiello, P., J. C. McWilliams, and A. Shchepetkin (2003), Equilibrium structure and dynamics of the California Current System, *J. Phys. Oceanogr.*, *33*(4), 753–783.
- Mikaloff-Fletcher, M., et al. (2006), Inverse estimates of anthropogenic CO<sub>2</sub> uptake, transport, and storage by the ocean. *Global Biogeochem. Cycles*, *20*, GB2002, doi:10.1029/2005GB002530.
- Najjar, R. G., and Orr, J. C. (1999), Biotic-HOWTO. Internal OCMIP Report, LSCE/CEA Saclay, Gif-sur-Yvette, France, 15 pp.
- Pennington, J. T., C. G. Castro, C. A. Collins, W. W. IV Evans, G. E. Friederich, R. P. Michisaki, and F. P. Chavez (2009), The northern and central California coastal upwelling system, chapter 2.2, in *Carbon and Nutrient Fluxes in Continental Margins*, Global Change – The IGBP Series, vol. 25, edited by K.-K. Liu et al., pp. 29–44, Springer-Verlag, Berlin, Heidelberg, doi:10.1007/978-3-540-92735-22.
- Renault, L., B. Dewitte, P. Marchesiello, S. Illig, V. Echevin, G. Cambon, M. Ramos, O. Astudillo, P. Minnis, and J. K. Ayers (2012), Upwelling response to atmospheric coastal jets off Central Chile: A modeling study of the October 2000 event, *J. Geophys. Res.*, *117*, C02030, doi:10.1029/2011JC007446.
- Resplandy, L., M. Lévy, F. d'Ovidio, and L. Merlivat (2009), Impact of submesoscale variability in estimating the air-sea CO<sub>2</sub> exchange: Results from a model study of the POMME experiment, *Global Biogeochem. Cycles*, *23*, GB1017, doi:10.1029/2008GB003239.
- Sabine, C. L., et al. (2004), The oceanic sink for anthropogenic CO<sub>2</sub>, *Science*, *305*(5682), 367–371.
- Shchepetkin, A. F., and J. C. McWilliams (2005), The regional oceanic modeling system (ROMS): A split-explicit, free-surface, topography-following-coordinate oceanic model, *Ocean Model.*, *9*, 347–404.
- Takahashi, T., S. C. Sutherland, R. A. Feely, and R. Wanninkhof (2006), Decadal change of the surface water pCO<sub>2</sub> in the North Pacific: A synthesis of 35 years of observations. *J. Geophys. Res.*, *111*, C07505, doi:10.1029/2005JC003074.
- Takahashi, T., S. C. Sutherland, and A. Kozyr (2013), Global ocean surface water partial pressure of CO<sub>2</sub> database: Measurements performed during 1957–2012 (version 2012), ORNL/CDIAC-160, NDP-088(V2012). Carbon Dioxide Information Analysis Center, Oak Ridge National Laboratory, U.S. Department of Energy, Oak Ridge, Tenn., doi:10.3334/CDIAC/OTG.NDP088(V2012).
- Taylor, K. E. (2001), Summarizing multiple aspects of model performance in single diagram, *J. Geophys. Res.*, *106*(D7), 7183–7192.
- Turi, G., Z. Lachkar, and N. Gruber (2013), Spatiotemporal variability and drivers of pCO<sub>2</sub> and air-sea CO<sub>2</sub> fluxes in the California Current System: An eddy-resolving modeling study, *Biogeosci. Discuss.*, *10*, 14,043–14,091, doi:10.5194/bgd-10-14043-2013.
- van Geen, A., R. K. Takesue, J. Goddard, T. Takahashi, J. A. Barth, and R. L. Smith (2000), Carbon and nutrient dynamics during coastal upwelling off Cape Blanco, Oregon, *Deep Sea Res. Part II*, *47*, 975–1002.
- Veneziani, M., C. A. Edwards, J. D. Doyle, and D. Foley (2009), A Central California coastal ocean modeling study: 1. Forward model and the influence of realistic versus climatological forcing, *J. Geophys. Res.*, *114*, C04015, doi:10.1029/2008JC004774.
- Wanninkhof, R. (1992), Relationship between wind speed and gas exchange over the ocean, *J. Geophys. Res.*, *97*(C5), 7373–7382.
- Weiss, R. (1974), Carbon dioxide in water and seawater: The solubility of a non-ideal gas, *Mar. Chem.*, *2*(3), 203–215.